nature communications

Article

https://doi.org/10.1038/s41467-025-63927-9

Soft bioelectronics embedded with self-confined tetrahedral DNA circuit for high-fidelity chronic wound monitoring

Received: 8 January 2025

Accepted: 1 September 2025

Published online: 07 October 2025

Check for updates

Xiao Zhao[1], Jiahao Huang[1], Juncheng Zhang[1], Bowen Yang[1], Zijuan Hu[1], Ting Li[1], Xiang Ma[2], Chunyan Jiang[2], Haochen Zou[1], Songrui Liu[1], Qiusui He[1], Lixing Weng[1], Ting Wang[1] ✉ & Lianhui Wang[1] ✉

Monitoring wound protein biomarkers, especially inflammation-related proteins, is essential to assess wound progression and guide treatment. However, high-fidelity wound biosensing is challenging because of current biosensors' limitations in detecting low-abundance proteins and their vulnerabilities to mechanical deformation, biofouling, and performance degradation. Here, we introduce a soft bioelectronics embedded with Self-Confined Tetrahedral DNA circuit (SCTD) for wound monitoring. In SCTD, proteins in wound exudate trigger DNA self-circulation amplification confined in the hydrophilic area, decreasing detection limits by an order of magnitude. The tetrahedral DNA structure ensures excellent mechanical stability (within 3% variation after 1000 bending cycles), prolonged stability (within 8% signal attenuation over 4 weeks), and reduced biofouling (over 50% BSA adhesion reduction). Coupled with wireless readout, this platform simultaneously monitors multiple wound healing-related proteins (TNF-α, IL-6, TGF-β1, and VEGF) and biophysical parameters. The wireless platform demonstrates accurate *in-situ* monitoring of both non-infected and infected wounds on diabetic male mice without hindering the healing process, offering quantitative and comprehensive evaluation to guide treatment.

Wound healing involves four sequential stages: hemostasis, inflammation, proliferation, and remodeling. Chronic wounds are often stuck in the proinflammatory phase[1–3]. Monitoring the healing phase, especially the inflammatory status, will benefit clinicians in assessing wound progression and guiding timely treatment decisions. Current clinical wound assessments rely on expensive instruments, cumbersome procedures, and experienced operators, hindering real-time diagnosis, patient rehabilitation, and efficient medical resource allocation[4,5]. Wearable wound biosensors, which integrate digital health techniques with flexible electronics, offer continuous, real-time, and in-situ tracking of physiological signs of wounds[6–9]. Although flexible sensors for wound monitoring have been extensively developed, they primarily detect biophysical signals such as temperature, pH, impedance, and pressure, as well as small metabolite molecules such as glucose, lactate, and uric acid[10–12]. Besides these limited biomarkers, many proteins, including cytokines and growth factors, play crucial roles in coordinating and regulating cellular and tissue responses to ensure effective healing. Stage-specific variations in the concentration of these low-abundance protein biomarkers can accurately indicate the healing stage and condition of wounds

[1]State Key Laboratory of Flexible Electronics (LoFE) and Jiangsu Key Laboratory of Smart Biomaterials and Theranostic Technology, Institute of Advanced Materials (IAM), Nanjing University of Posts and Telecommunications, Nanjing, China. [2]State Key Laboratory of Reproductive Medicine and Offspring Health, Clinical Center for Reproductive Medicine, First Affiliated Hospital of Nanjing Medical University, Nanjing, China. ✉e-mail: iamtingwang@njupt.edu.cn; iamlhwang@njupt.edu.cn

(Supplementary Fig. 1)[3,13,14], providing integrated information on cellular activities, tissue regeneration, and immune responses. These will benefit a thorough understanding of the biological processes involved in wound healing, thus supporting informed treatment decisions.

Despite the above advantages for in-situ detection of wound healing-related proteins, several challenges should be resolved toward practical wound assessment. Firstly, wound healing-related proteins are present in low abundance, while signal amplification for sensitive detection on soft interfaces remains difficult without extra operations or external reagent triggers[15–18]. This is particularly challenging when multiple biomarkers are needed to be detected to accurately monitor the healing stage. Secondly, biosensing under wound conditions faces critical challenges in fidelity: structural compromise from motion-induced deformation, non-specific protein fouling, and sensing element degradation caused by the complex biochemical environment (e.g., nucleases), all of which lead to decreased biosensing fidelity[5,19,20]. Lastly, wounds impose rigorous requirements on the biosensing patch in terms of permeability, compliance, and biocompatibility, as the patch should not cause physical damage and inflammation or impede the wound-healing process[11,21,22]. To address substrate-related issues, electrospun nanofibers[23–25] with high porosity offer an ideal platform due to their excellent breathability and mechanical flexibility for wound-interfaced applications, while such breathable biosensor has not been achieved yet.

In response to the aforementioned challenges, we develop Self-confined Tetrahedral DNA Circuit (SCTD) embedded breathable and soft electronics for comprehensive monitoring of various stage-specific proteins and biophysical indicators of the wound (Fig. 1a). Key indicators, including tumor necrosis factor-α (TNF-α), interleukin-6 (IL-6), transforming growth factor-β1 (TGF-β1), and vascular endothelial growth factor (VEGF), reflect different healing statuses of chronic wounds. To ensure the gas permeability and softness of biosensors, we exploit electrospun polyacrylonitrile/thermoplastic polyurethane (PAN/TPU) nanofibers with defined hydrophilic biosensing area as the substrate. The soft, breathable, and patterned wettable nanofiber-based patch enriches wound exudate and prevents reagent diffusion, creating a hydrophilic biosensing reaction pool without impeding wound healing (Fig. 1b). Within the biosensing pool, SCTD achieves target-triggered signal amplification through a combination of exogenous auxiliary nucleic acid pre-coating strategy and spatial confinement, enabling sensitive detection of trace biochemical markers (Fig. 1c). Compared to traditional single strand DNA (ssDNA)-based protein sensors, the rigid tetrahedral DNA (TDNA) ensures stable electrochemical signal generation even under bending conditions. Furthermore, the inherent anti-degradation and antifouling properties of the TDNA prevent degradation of biosensing elements and biofouling in the complex wound microenvironment, exhibiting long-term stability for up to four weeks. By integrating biochemical and biophysical sensing arrays, a wireless flexible printed circuit board (FPCB), and a smartphone-based user interface, this breathable sensing system allows for in-situ, real-time, sensitive, and stable monitoring of multiple physiological indicators at the wounds of diabetic mice, without impeding the healing (Fig. 1d, e and Supplementary Table 1). This biosensing platform can facilitate a comprehensive assessment and provide treatment guidance for chronic wounds.

Results

Design and overview of the integrated wearable biosensing system

The integrated wearable biosensing system consists of a multimodal biosensing array and a miniaturized FPCB for signal processing and wireless communication with the user interfaces (Fig. 1a). During wound healing, cells release inflammatory cytokines, including tumor necrosis factor-α (TNF-α) and interleukin-6 (IL-6) to initiate the inflammatory response. As healing progresses, there is a gradual elevation in the concentration of anti-inflammatory factors, exemplified by transforming growth factor-β1 (TGF-β1), marking the transition to the anti-inflammatory and repair phase[26]. Additionally, the concentration of growth factors, particularly vascular endothelial growth factor (VEGF), essential for angiogenesis and tissue repair, increases during the wound healing process[27] (Fig. 1a). To capture these dynamic changes, a multimodal biosensor array was integrated into the wireless system for simultaneous detection of wound healing-related proteins and biophysical parameters, reflecting the state and stage of wound healing, without causing physical damage or impeding the healing process (Fig. 1b).

Nucleic acid-based signal amplification strategies, including polymerase chain reaction, loop-mediated isothermal amplification, and hybridization chain reaction, are extensively used in laboratory diagnostics to enhance sensitivity[28–30]. These strategies generally require the involvement of large instruments, high temperatures, and auxiliary reagents, which limits their application on body surfaces or in vivo[31]. Recent advances have attempted to address these limitations by integrating DNA amplification technologies into wearable platforms where optical readout methods are involved to ensure high sensitivity[32–34]. To date, existing approaches fail to address the unique requirements of wound monitoring, which demands breathable substrates to prevent wound maceration, mechanical stability to withstand body movements, and instrument-free operation for continuous bedside monitoring. To meet these specific requirements in the wound monitoring scenarios, we designed an SCTD approach based on a self-confined, DNA cascade amplification pool with an auxiliary nucleic acid pre-coating strategy. The expected advantages include: (1) confined autonomous amplification without external reagents, (2) mechanical adaptability with breathable and bending-stable substrates, and (3) electrochemical output for seamless system integration. This integrated design enables truly autonomous and reagent-free monitoring directly at the wound interface.

To effectively capture the dynamic biochemical clues based on low-abundance proteins in wounds, we intend to introduce a signal amplification method based on nucleic acid technology for wearable wound sensors. The key mechanism lies in the “self-confined” design, where amplification reactions are autonomous spatially restricted within designated hydrophilic regions through surface tension effects. Specifically, the confined reaction pool is achieved through hydrophilic patterning of the nanofiber patch where the hydrophilic areas serve as reservoirs for auxiliary hairpin DNA (H1) while surrounding hydrophobic areas prevent H1 diffusion (Fig. 1b). The hydrophilic biochemical biosensing areas were modified with TDNA via Au-S bonding and pre-coated with H1 dry powder containing a target-specific recognition aptamer sequence ((1) in Supplementary Fig. 2). Upon the wound exudate gathered in the hydrophilic area, the H1 dry powder dissolves and captures target proteins in the exudate ((2) in Supplementary Fig. 2). The unfolded H1 modified with methylene blue (MB) signal molecule exposes the sticky end and opens the hairpin located on the top of TDNA (H2), decorating MB on the biosensing electrode according to the concentration relationship of the target ((3) in Supplementary Fig. 2). Due to the higher affinity between H1-H2 compared to H1-target, the protein is released from the intermediate and circularly participates in a cascade reaction with H1 and H2, enabling a recyclable utilization of the target ((4) in Supplementary Fig. 2). Such a confined DNA-based signal amplification pool enables sensitive monitoring of low-abundance wound proteins. Moreover, the biophysical sensing area was designed to obtain comprehensive information about wound healing, including polyaniline (PANI)-based pH sensing electrodes and metal microwire-based temperature sensors.

https://doi.org/10.1038/s41467-025-63927-9

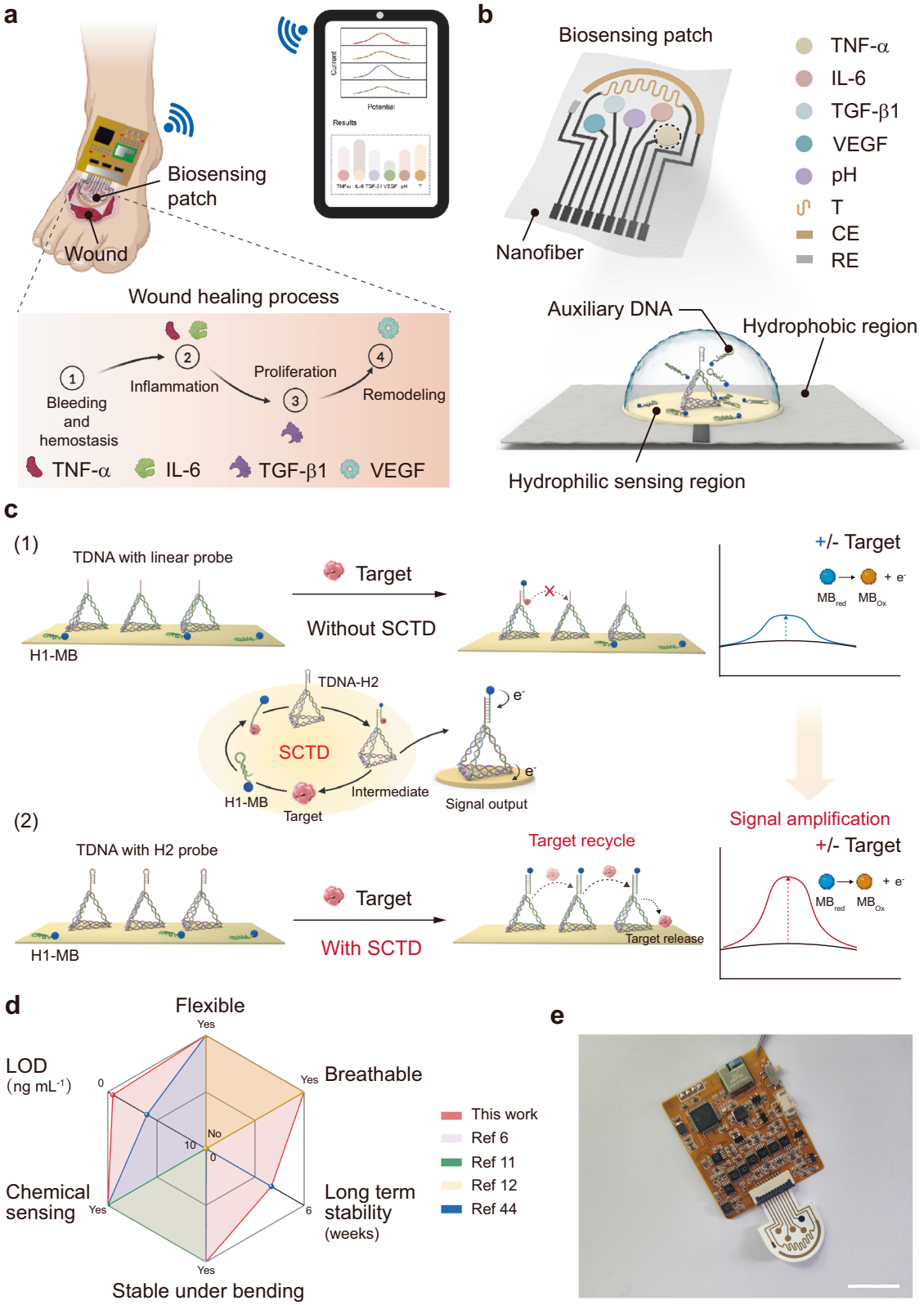

Characterization of the nanofiber-based self-confined DNA reaction pool

The properties of the nanofiber-based substrate are essential for constructing a sensing system that minimally obstructs wound healing while enabling SCTD. To ensure good breathability, heat dissipation, and softness in the wound healing environment, electrospinning of biocompatible TPU and PAN were utilized to fabricate porous nanofiber substrate for the wound biosensing electronic (Fig. 2a). The nanofiber was successfully produced, featuring a porous structure formed by interwoven fibers, as confirmed by the scanning electron microscopy (SEM) image (Fig. 2b). With an optimal TPU to PAN mass ratio of 1:1, the nanofiber exhibited a uniform diameter of 110 nm without bead formation and softness (Supplementary Fig. 3 and Supplementary Fig. 4). To fabricate conductive biosensing regions on the

Fig. 1 | Wearable soft biosensing bioelectronic system based on nucleic acid cascade amplification for *in-situ* chronic wound monitoring. a Schematic of a wearable, breathable, and wireless FPCB on a chronic diabetic foot wound; wound healing mechanism and different wound healing-related proteins released in different stages of wound healing. Created in BioRender. Xiao, X. (2025) https://BioRender.com/z38470w. **b** Top: Schematic illustration of the nanofiber-based multiplexed biosensing electronics, which comprises biophysical and biochemical sensors for pH, temperature, and wound healing-related proteins detection. Bottom: DNA solution confined in the hydrophilic region of the nanofiber based on patterned wettability. T temperature, CE counter electrode, RE reference electrode. **c** Schematic comparison of DNA circuit reactions and sensing signals triggered by target with (2) and without (1) SCTD, along with illustration of SCTD working principle: In hydrophilic-confined regions, target proteins in wound exudate trigger DNA cascade amplification around electrode-anchored TDNA, with pre-coated auxiliary DNA (H1) dissolution enabling the amplification process. **d** Radial graph comparing different wearable wound sensors based on various properties[6,11,12,44]. Source data are provided as a Source Data file. **e** Digital images of a fully integrated wireless bioelectronic system. Scale bar, 2 cm.

non-conductive nanofiber, a gold electrode array was deposited onto the nanofiber via thermal evaporation using shadow masks (Fig. 2c). The DC resistance of Au/nanofiber reveals negligible changes within 4% variation during 2000 bending cycles, confirming excellent electrical stability under mechanical deformation (Supplementary Fig. 5). Furthermore, cyclic voltammetry (CV) and electrochemical impedance spectroscopy (EIS) measurements conducted before and after 1000 bending cycles (bending radius: 3 cm) demonstrated excellent electrochemical stability, with <1% variation in redox peak currents and peak potential separation, and <8% change in charge transfer resistance, confirming stable electrochemical performance under mechanical deformation (Supplementary Fig. 6). Besides, the gas permeability, measured by the water vapor transmittance rate (WVTR) following the American Society for Testing Materials E96 upright cup standard[35,36], revealed that nanofiber-based substrate (TPU:PAN = 1:1, mass ratio) exhibited the highest gas permeability (WVTR: 110 g m^{-2} h^{-1}) compared to other nanofiber substrate (TPU:PAN = 1:2 and 2:1) with different TPU to PAN ratio (WVTR: 88.2 and 97 g m^{-2} h^{-1}, respectively), PDMS (WVTR: 41 g m^{-2} h^{-1}), and commercial wound dressing (WVTR: 91 g m^{-2} h^{-1}) (Fig. 2d). This level of breathability meets the breathability requirements of human skin[37]. Additionally, infrared thermal images (Fig. 2e) showed similar temperature change between bare skin (33.0 °C) and nanofiber-covered skin (33.3 °C), whereas commercial wound dressings (34.4 °C) and PDMS (34.6 °C) showed elevated temperatures, suggesting satisfactory heat dissipation of the nanofiber-based biosensing patch. These features - mechanical flexibility, breathability, and efficient heat dissipation - ensure that the nanofiber-based substrate creates an ideal platform for biosensor integration without compromising the wound healing environment.

To realize SCTD on the nanofiber, hydrophilic biosensing reaction pools were constructed to confine auxiliary nucleic acid strands. The patterned wettability on the nanofiber was achieved through hydrophobic reagent and oxygen plasma techniques (Fig. 2f). Contact angle measurements confirmed the hydrophobic nature of hydrophobic reagent-treated nanofiber (107°). Optimal oxygen plasma treatment with optimized parameters of 200 W for 30 seconds significantly reduced the contact angle to 49° (Supplementary Fig. 7), creating an effective hydrophilic surface without altering the fiber structure (Supplementary Fig. 8). A methyl orange aqueous solution was employed to visually characterize the patterned wettability and distinguish the hydrophilic and hydrophobic regions of the nanofiber. Water droplets selectively wetted the circular (Supplementary Fig. 9) and fox-shaped (Fig. 2g) hydrophilic areas and were repelled by hydrophobic regions, forming a well-defined shape under both flat and bending conditions. Notably, this patterning approach achieved a resolution of 500 µm for wettability features (Supplementary Fig. 10). Furthermore, the fluorescence image confirmed that fluorophore-labeled H1 was confined to the hydrophilic regions without diffusing in the patterned wettability nanofiber, ensuring the biosensing amplification circuit operates in the biosensing pool (Fig. 2h, i). In order to avoid premature termination of the sensing reaction due to solution evaporation, we characterized the solution on different nanofibers. A series of time-lapse images showing the patterned wettable nanofiber can keep for a longer time (2700 s) than the untreated nanofiber (60 s) without drying up in an open environment (Supplementary Fig. 11).

Validation of the advantages of tetrahedral DNA-based signal amplification circuit

For accurate detection of low-abundance proteins in wound exudate, signal amplification strategies are highly desired. Traditional nucleic acid amplification strategies typically rely on external reagents and large-scale instruments, hindering the application of *in-situ* and real-time biosensing on biointerfaces[38–40]. To overcome the limitations, an SCTD strategy was adopted for sensitive, on-site, and real-time detection of wound healing-related biomarkers. TDNA nanostructures, a well-established biosensing platform, have been reported to exhibit superior mechanical properties compared to linear DNA structures[41–43], making them suitable for soft biosensing devices that experience mechanical deformation during wound monitoring. In the SCTD strategy, the tetrahedral scaffold is functionalized with a hairpin DNA sequence (H2) at its apex, while auxiliary hairpin DNA (H1) modified with MB is pre-coated as dry powder in the hydrophilic sensing region (Fig. 1c). Upon target binding to H1, conformational changes expose complementary sequences that enable hybridization with H2. The mechanism to signal amplification lies in the engineered binding affinities: H1-H2 interaction is designed to be stronger than H1-target binding, allowing target molecules to be released and participate in multiple reaction cycles ((2) in Fig. 3a). This recyclable target utilization dramatically enhances signal generation, with MB molecules oxidized at approximately −0.28 V[44,45] for electrochemical detection by square wave voltammogram (SWV). In contrast, in the control tetrahedral DNA sensors without amplification, the H1-target binding is stronger than H1-linear probe interactions, causing targets remain bound to H1, resulting in limited MB decoration on the electrode ((1) in Fig. 3a). The SCTD strategy, combined with the inherent advantages of the tetrahedral DNA framework, enables sensitive detection of low-abundance proteins while maintaining excellent mechanical stability and antifouling performance.

TDNA self-assembly was validated through native polyacrylamide gel electrophoresis (PAGE) analysis (Fig. 3b). Detailed information for DNA sequences is given in Supplementary Table 2. To verify the feasibility of the SCTD strategy, the H2 sequence was extracted from TDNA and tagged fluorophore (FAM) and quencher (BHQ-1) at both ends of H2. Due to the hairpin structure of H2, fluorophore and quencher are in close proximity, resulting in no fluorescence signal[46,47]. In the absence of target, H2 and H1 coexist stably without hybridization, yielding no fluorescence signal. Once the target was introduced, H1 can bind to the target and expose the sticky end, thereby opening the hairpin structure of H2, leading to the separation of the fluorophore and quencher to generate a fluorescence signal[48,49] (Fig. 3c).

Electrochemical tests further validated the SCTD strategy, showing signal generation only when H1, H2, and the target were present simultaneously (Fig. 3d). Here, SWV was selected for electrochemical measurements due to its superior sensitivity for MB redox signal detection through effective discrimination between faradaic and capacitive currents[50,51], and its demonstrated better performance compared to Differential Pulse Voltammetry for DNA-based electrochemical sensors (Supplementary Fig. 12). To understand the electrochemical behavior of H1 in different states, we conducted control experiments examining H1-MB in various conformations. When H1-MB exists in its hairpin conformation alone, it exhibits negligible oxidation

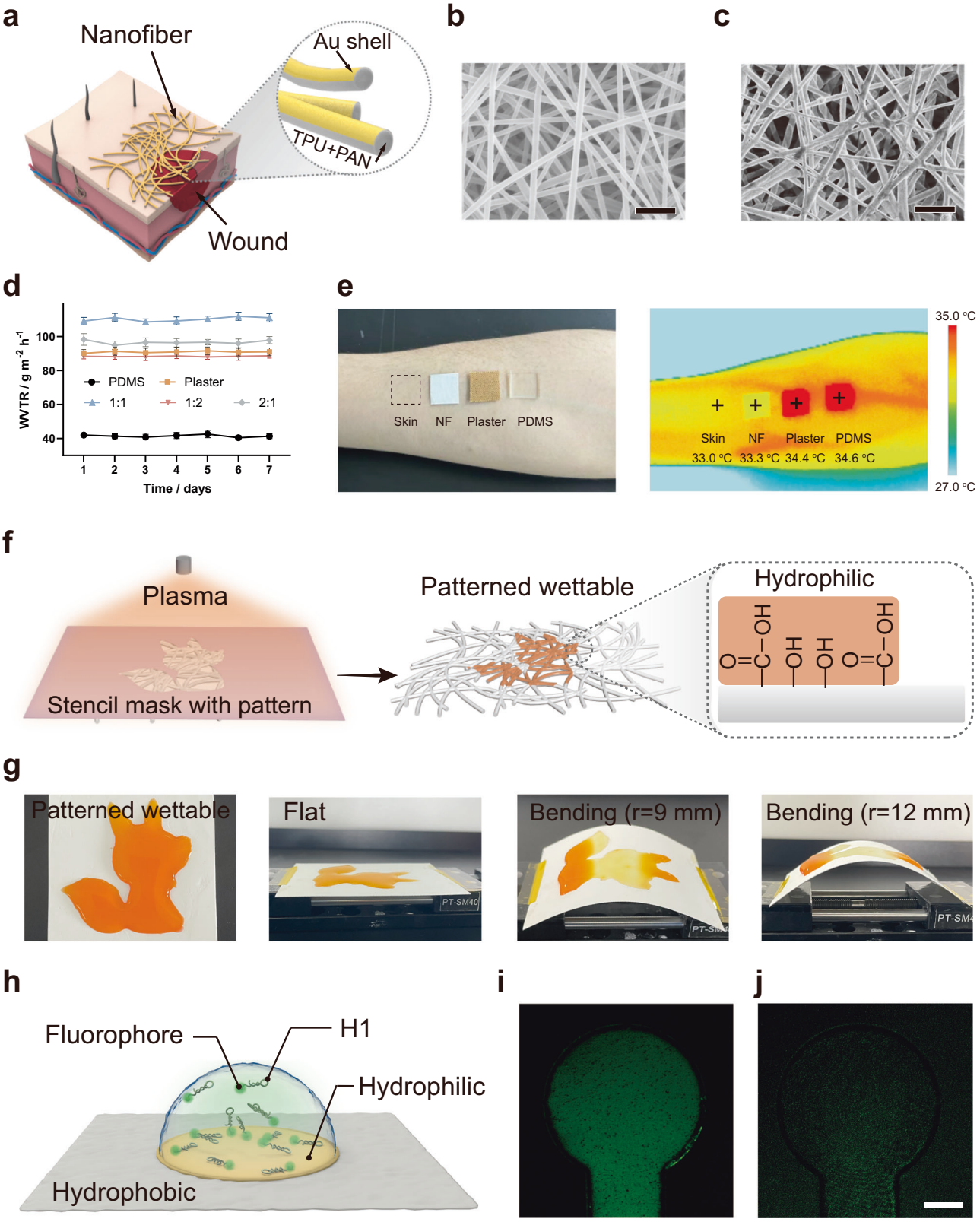

peak current (0.08 μA at −0.28 V), suggesting that the folded hairpin structure may prevent efficient electron transfer between MB and the electrode surface (Supplementary Fig. 13). Upon linearization of the H1-MB structure by complementary sequences (H1′), the oxidation peak current increases to 0.34 μA (4.3-fold enhancement), while the complete SCTD system with target proteins (IL-6) achieves 3.2 μA (40-fold enhancement over the hairpin state). These results demonstrate that the hairpin structure effectively "silences" the electrochemical signal until target-triggered conformational changes occur. To evaluate the effectiveness of the SCTD strategy for detecting low-concentration targets, we compared the response of sensors to different concentrations of IL-6 with and without signal amplification. Results showed that the sensor with signal amplification exhibited higher responses (Fig. 3e and Supplementary Fig. 14) and achieved the

Fig. 2 | Characterizations of the nanofiber-based self-confined DNA reaction pool. a Schematic illustration of the nanofiber-based substrate adhered onto a chronic wound. SEM images of electrospun nanofiber before (**b**) and after (**c**) gold deposition. Scale bar, 2 μm. The experiment was independently repeated three times with similar results. **d** The comparison of WVTR between different materials ($n = 3$ independent experiments). Data are presented as mean ± SD. Source data are provided as a Source Data file. **e** The comparison of optical and infrared thermal images between different wound dressings. NF nanofiber. Explicit consent for the publication of images was obtained from the participant. The experiment was independently repeated three times with similar results. **f** Schematic diagram illustrating the fabrication process for patterned wettability on nanofibers through plasma treatment. **g** Optical images showing absorbed methyl orange solution confined to the fox pattern under different radii of curvature. The experiment was independently repeated three times with similar results. **h** Schematic diagram of the fluorophore-labeled H1 confined in the hydrophilic region of the patterned wettable material. Representative fluorescence images show the comparison of DNA solution confined in the hydrophilic region of the patterned wettable nanofiber (**i**) and the untreated nanofiber (**j**). Scale bar, 700 μm. The experiment was independently repeated three times with similar results.

low limit of detection (LOD) (0.52 ng mL^{-1}), one order of magnitude lower than that without amplification (4.26 ng mL^{-1}) (Supplementary Fig. 15).

In order to adapt to the deformation of wearable biosensing electronic, we also compared the fidelity between traditional aptamer (an ssDNA)-based biosensing element and TDNA-based biosensing element on the same electrode substrate (Fig. 3f-i and Supplementary Fig. 16). ssDNA-based sensor showed increased peak currents after bending 1000 cycles (increasing ratio: 36%) (Fig. 3g), which is possibly due to the conformational changes of ssDNA (Fig. 3f). In contrast, TDNA-based sensors maintained stability after bending 1000 cycles (decreasing ratio: 2.7%) benefits from the rigid tetrahedral structure, suggesting robustness under bending (Fig. 3h, i). This high mechanical stability is further validated by sensing TNF-α, IL-6, TGF-β1, and VEGF using TDNA structures, which show variations within 3% under 1000 bending cycles (Supplementary Fig. 17). This indicates that the TDNA-based sensor can maintain its performance under bending deformation, making it suitable for continuous wound monitoring.

Biosensing array needs to operate in complex fluid, where non-specific adsorption can reduce sensitivity and specificity, the inherent antifouling property of TDNA can reduce the adsorption of bovine serum albumin (BSA) (Fig. 3j). Confocal laser scanning microscopy (CLSM) imaging revealed that TDNA-based gold electrodes exhibited substantially reduced BSA adsorption compared to both bare gold electrodes and ssDNA-modified gold electrodes (Fig. 3k). Quantitative analysis showed that the TDNA-modified electrodes achieved a significantly lower BSA adhesion rate (6.9%) compared to ssDNA-based biosensing electrodes (26.2%) and bare Au electrodes (39.2%) (Fig. 3l, m). This enhanced antifouling performance can be attributed to the increased surface hydrophilicity of TDNA-modified electrodes[52,53] relative to both single-strand aptamer-based sensing electrodes and bare Au electrodes (Fig. 3n), consistent with established correlations between surface hydrophilicity and antifouling properties[54,55].

Considering the DNA degradation due to the potential existence of nucleases in aqueous wound conditions, we investigate the anti-degradability of TDNA- and ssDNA-based sensors through long-term stability tests in buffer solutions with potential nucleases. The ssDNA-based sensors exhibited an 868% signal increase after four weeks (Supplementary Fig. 18), likely due to aptamer degradation, which shortened the distance between the signal molecule and the electrode. In contrast, the TDNA-based sensor showed less than 8% signal attenuation over the same period (Supplementary Fig. 19) due to its inherent structural stability[42,56,57]. Collectively, these comprehensive characterizations demonstrate that TDNA-based electrodes outperform traditional ssDNA-based sensors in terms of LOD, antifouling, anti-bending, and antidegradation capabilities (Fig. 3o). These superior properties ensure reliable protein detection under complex wound environments, which is crucial for accurate wound assessment.

Performance and evaluation of in-vitro multiplexed biosensing electronic

To detect low-abundance wound-associated proteins, our sensor incorporates the SCTD strategy on the biosensing electronics (Fig. 4a, b). The fabrication process involves sequential steps including nanofiber electrospinning, gold electrode deposition, patterned wettability treatment, TDNA functionalization, and sensor array integration, as illustrated in the detailed fabrication schematic (Supplementary Fig. 20). As the first step in implementing this strategy, an optimal amount (10 μL of 600 nM) of TDNA (Supplementary Fig. 21) was immobilized on the electrode surface overnight via Au-S formation. Subsequently, inactive sites on the electrode surface were blocked using 10 μL of 1 mM MCH, followed by drop-casting the optimal amount (10 μL of 1.5 μM) of H1 (Supplementary Fig. 22) onto the MCH/TDNA/Au/ nanofiber electrode to create pre-coated H1 dry powder. The successful fabrication of the H1/MCH/TDNA/Au/nanofiber biosensing electrode was verified by CV and EIS after each modification step, using $Fe(CN)_6^{3-/4-}$ as the electrochemical probe (Supplementary Fig. 23). The CV curve demonstrated that the Au/nanofiber electrode had the highest redox peak currents and smallest peak potential difference, indicating an accelerated electron transfer rate. Similarly, Nyquist plots demonstrated that the Au film reduced the charge transfer resistance, enhancing electron transfer kinetics at the electrode interface[58]. A gradual decrease in electron transfer rate after stepwise modification with non-conductive DNA and MCH further verified the successful preparation of H1/MCH/TDNA/Au/nanofiber electrode[59]. Besides, the optimal times for detection of TNF-α, IL-6, TGF-β1, and VEGF were determined to be 40, 50, 50, and 50 min, respectively (Supplementary Fig. 24), which ensures complete target recognition, H1-H2 interaction, intermediate conformational change, and target recycling to achieve sufficient DNA cascade amplification for low-abundance protein detection.

The biochemical sensing performance was evaluated in artificial wound fluid (AWF) (Fig. 4c–g). The sensor exhibited linear responses within clinically significant concentration ranges[44,60] for TNF-α (10–5000 pg mL^{-1}), IL-6 (1–100 ng mL^{-1}), TGF-β1(1–100 pg mL^{-1}), and VEGF (0.05–20 ng mL^{-1}). The sensors achieved impressive analytical performance with low LODs (TNF-α: 3.67 pg mL^{-1}, IL-6: 0.52 ng mL^{-1}, TGF-β1: 0.41 pg mL^{-1}, VEGF: 6.3 pg mL^{-1}) and high correlation coefficients ($R^2 > 0.98$). The LODs were calculated as three times the standard deviation of the blank divided by the slope of the calibration curve ($S/N = 3$). The accuracy was validated against a commercial ELISA kit for TNF-α detection (Fig. 4h, i), showing a good correlation ($R^2 = 0.98$) between the two methods. Thanks to the high affinity of aptamer in H2, our sensors demonstrated excellent selectivity and reproducibility (Supplementary Fig. 25).

Characterizations of the biophysical sensing modules

In the wound healing process, temperature and pH are also biophysical indicators. Briefly, elevated wound temperature suggests potential infection, inflammation, and compromised healing[61,62]. Additionally, optimal healing conditions are associated with a slightly acidic pH, promoting collagen formation, fibroblast activity, and inhibiting bacterial growth, while an alkaline pH (7-9) signifies impaired healing[63,64].

Accordingly, we incorporated temperature and pH sensing modules into the sensing platform (Fig. 4b). The PANI-based pH sensor was measured as a function of the open-circuit potential (OCP) changes resulting from protonation/deprotonation on the PANI surface. Within the pH range of 4–10, OCP linearly decreases with increasing pH,

https://doi.org/10.1038/s41467-025-63927-9

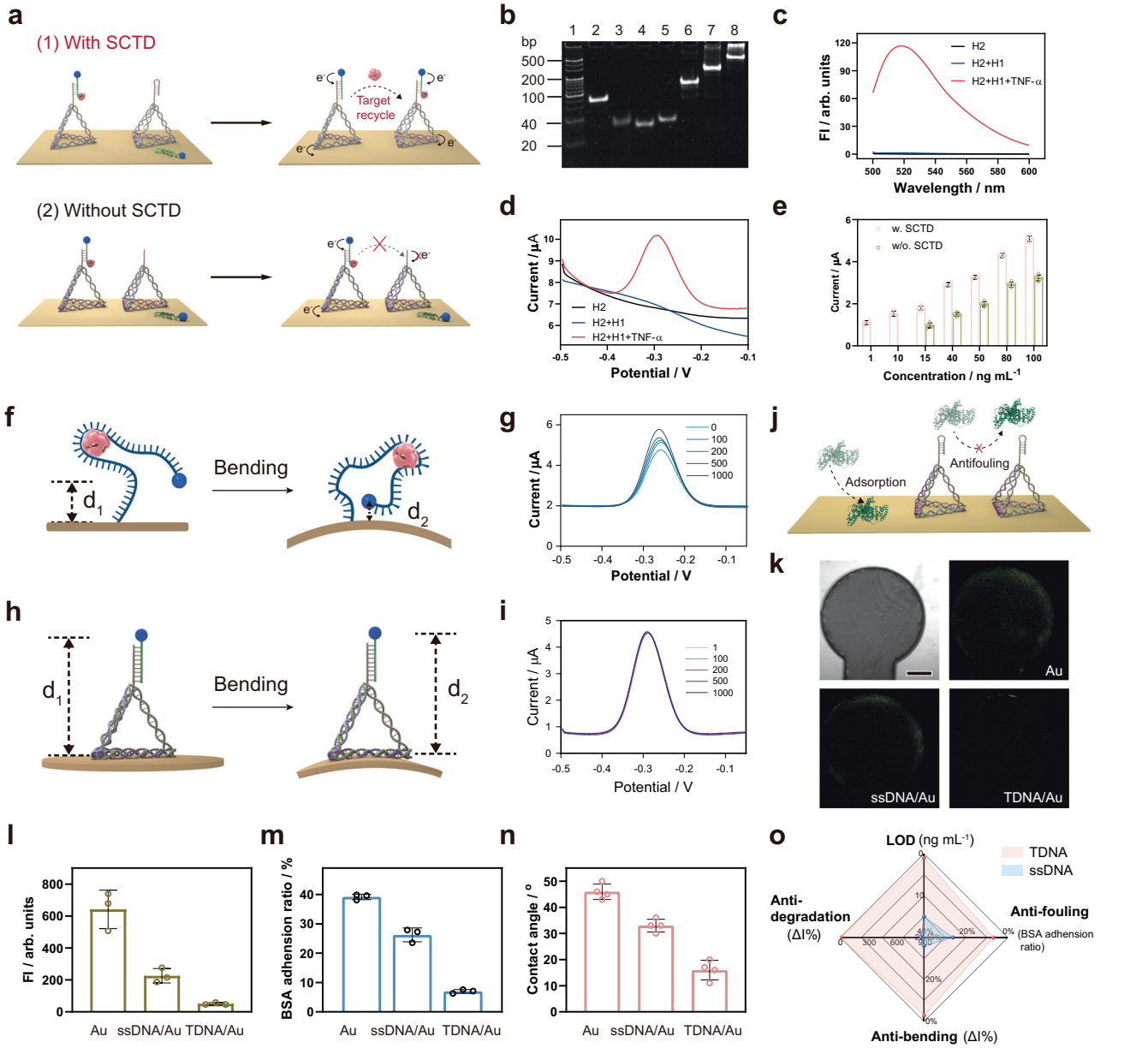

Fig. 3 | Validating the advantages of the Self-confined Tetrahedral DNA Circuit (SCTD) regarding signal amplification, enhanced mechanical stability, anti-fouling capability, and long-term stability. a Schematic illustration of the sensing mechanism with and without SCTD. **b** PAGE analysis showing the self-assembly of TDNA and various combinations of TDNA sequences. lane 1: marker (20–500 bp), lane 2: P1, lane 3: P2, lane 4: P3, lane 5: P4, lane 6: P1 + P2, lane 7: P1 + P2 + P3, lane 8: P1 + P2 + P3 + P4. This experiment was repeated three times independently with similar results. Fluorescent (**c**) and electrochemical (**d**) characterization of the feasibility of the biosensing strategy. **e** Calibration curve for the detection of IL-6 in the absence and presence of an amplification circuit ($n = 5$ independent experiments). Data are presented as mean ± SD. **f**–**i** Comparison of mechanical stability between ssDNA- and TDNA-based biosensing electrodes: schematic illustrations of structural deformation (**f**, **h**) and corresponding electrochemical signal variations (**g**, **i**) during 1000 bending cycles. Radius of bending curvature, 3 cm. **j** The schematic diagram illustrating the antifouling performance of TDNA against BSA. CLSM images (**k**) and corresponding fluorescence intensity (**l**) of different electrodes fouled in BSA-FITC for 3 h ($n = 3$ independent experiments). The experiment was independently repeated three times with similar results. Data are presented as mean ± SD. Scale bar, 500 μm. **m** Comparison of the BSA adhesion ratios by different electrodes measured by BCA assay ($n = 3$ independent experiments). Data are presented as mean ± SD. **n** Comparison of the water contact angles between different electrodes ($n = 4$ independent experiments). Data are presented as mean ± SD. **o** Radar plot demonstrating the superior performance of TDNA-based biosensors over ssDNA-based biosensors in LOD, antifouling, anti-bending, and antidegradation capabilities. Source data from (**b**–**e**, **g**, **i**, **l**–**o**) are provided as a Source Data file.

showing a sensitivity of −46 mV pH^{-1} and remains stable at constant pH (Fig. 4j). The temperature sensor, constructed with a thermally responsive resistor in a serpentine structure, was designed to withstand the stresses from daily activities at the wound. The temperature sensor shows a sensitivity of 1.4 Ω $°C^{-1}$, across a physiologically relevant range from 35 to 45 °C (Fig. 4k). Furthermore, temperature and pH sensors have been proven to have excellent stabilities under deformation and long-term stability (Supplementary Fig. 26).

Biocompatibility investigation and in-situ chronic wound biosensing in mice models

Prior to in-situ wound detection, the biocompatibility and hemocompatibility of the biosensing patch have been characterized. After 24 h of co-culture with the electrospun fiber-based biosensing patch, NIH/3T3 cells exhibited excellent viability without dead cells (Supplementary Fig. 27a). Hemocompatibility results demonstrated that the test group, with the electrospun fiber-based patch, showed

https://doi.org/10.1038/s41467-025-63927-9

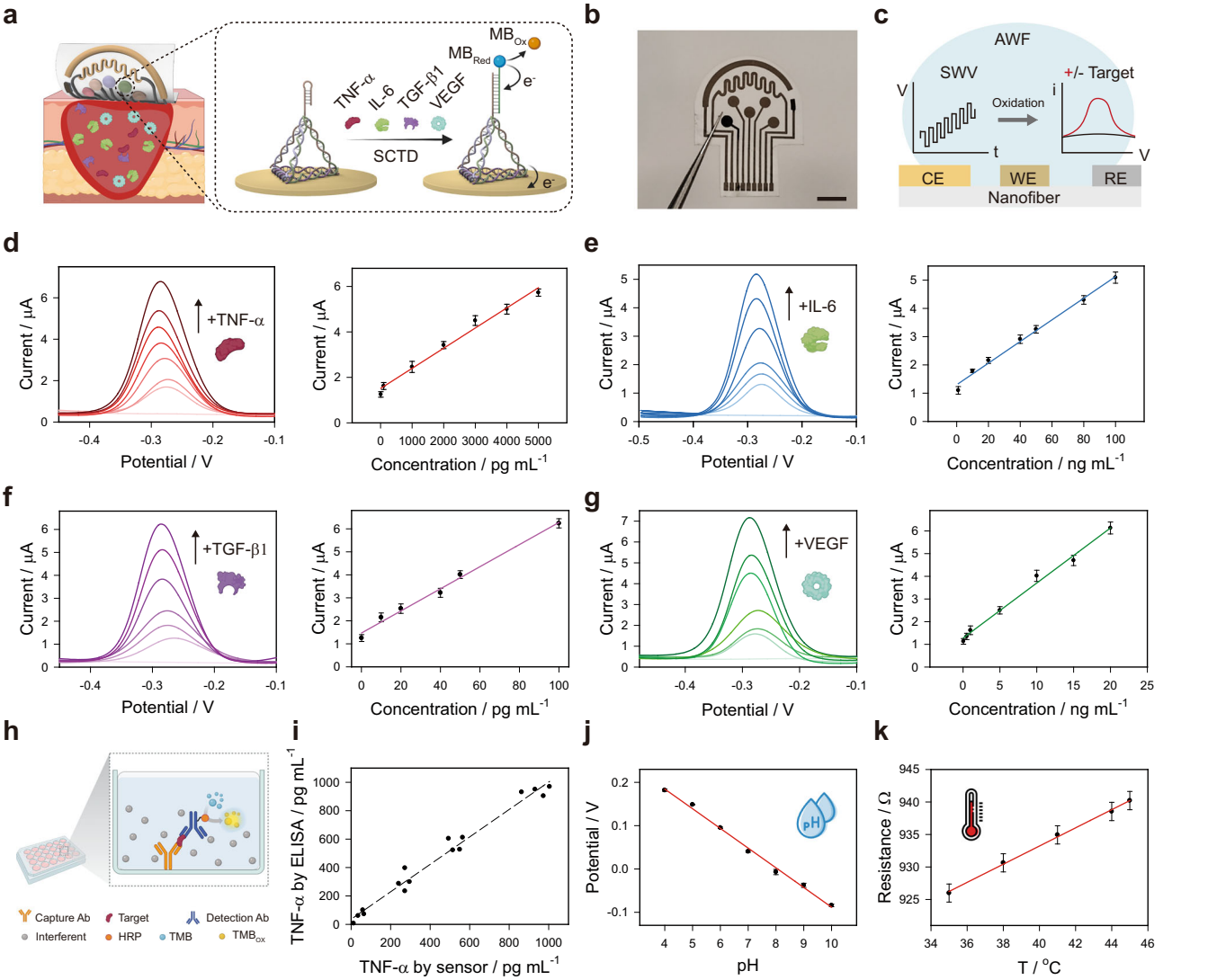

Fig. 4 | Schematics and characterizations of the multiplexed biosensor. **a** Illustration of wound-associated proteins released from the wound and the biochemical sensing mechanism. Created in BioRender. Xiao, X. (2025) https://BioRender.com/alwdc8p. **b** Digital photograph of a multiplexed sensing electrode. Scale bar, 1 cm. **c** A three-electrode nanofiber-based flexible sensor for the detection of protein biomarkers using SWV in AWF. CE, counter electrode; WE, working electrode; RE, reference electrode. SWV and calibration curves of TNF-α (**d**), IL-6 (**e**), TGF-β1 (**f**), and VEGF (**g**) in artificial wound fluid ($n = 3$ independent experiments). Data are presented as mean ± SD. **h** Schematic diagram illustrating the mechanism of the ELISA kit for detecting TNF-α. Created in BioRender. Xiao, X. (2025) https://BioRender.com/pqrm4ok. **i** Validation of the TDNA-based sensor towards TNF-α detection in AWF with ELISA. Calibration curve of the pH sensor (**j**) and temperature sensor (**k**) versus pH values and temperature values, respectively ($n = 5$ independent experiments). Data are presented as mean ± SD. Source data from (**d**–**g**, **i**–**k**) are provided as a Source Data file.

transparent supernatant similar to the PBS group, confirming the excellent blood compatibility of our biosensing patch (Supplementary Fig. 27b). To further validate the excellent biocompatibility of the biosensing patch at both non-infected and infected wounds on diabetic mice model, histological assessment was applied to the tissue where the cutted biosensing patch was attached (Fig. 5a and Supplementary Fig. 28a). Following placement of the biosensing patch on the wound surface for continuous monitoring, no redness or swelling was observed at the patched wound, and the healing rate was comparable to the control group (Fig. 5a–c, and Supplementary Fig. 28b, c). Besides, hematoxylin and eosin (H&E) tissue section images revealed no foreign body responses in either control or experimental groups (Fig. 5d). Furthermore, no significant difference in wound diameter and thickness of proliferating and upward-migrating basal keratinocytes was observed between the control and experimental groups (Fig. 5e). Additionally, immunofluorescence staining revealed that inflammatory cell infiltration in tissues with the cutted sensing patch was consistent with that in the control group (Fig. 5f).

Based on the satisfactory biosensing properties and biocompatibility of our designed patch, a fully integrated FPCB, including a wireless communication module and smartphone-based user interface, was incorporated into the sensing array to verify the ability to in-situ detect chronic wounds in mice (Fig. 5g–i). As depicted in Supplementary Fig. 29, we initiated diabetic mouse models by intraperitoneal injection of streptozotocin solution for 7 days starting from day −7. On day 0, wounds of identical size were incised at both sides of the mouse's back, making the two wounds equidistant from the central axis. The biosensing system was applied to the wound surface on the right side, while the left side remained untreated as the control group. Mice equipped with multi-channel sensors were observed to live freely without discomfort or excessive scratching (Fig. 5i and Supplementary Movie 1). Multiplexed sensor data were wirelessly collected and

https://doi.org/10.1038/s41467-025-63927-9

displayed via a user interface (Supplementary Fig. 30a and Supplementary Movie 2)

It is reported that during the wound healing process, TNF-α and IL-6 increase in the inflammatory status and decrease in the proliferation and remodeling statuses[65]. Meanwhile, the levels of anti-inflammatory factors and regenerative factors, notably TGF-β1 and VEGF, gradually rise in the proliferation and remodeling statuses[27,66]. In the diabetic wound model without bacterial infection, the first two days after wounding showed elevated levels of TNF-α and IL-6, indicating the onset of the inflammatory phase. As the concentrations of TNF-α and IL-6 gradually decrease while TGF-β1 and VEGF continue to rise, it signifies the transition to the proliferation and remodeling phases (Supplementary Fig. 30b). Additionally, the pH value decreases by 6% on day 4 compared to day 0 (Supplementary Fig. 30b),

Fig. 5 | Evaluation of the wearable sensor for in-situ monitoring of chronic infected wounds and biocompatibility in a diabetic mouse model. a Image of the cutted biosensing patch mounted on a skin wound in vivo. The cutted biosensing patch is in contact with the right wound, while the left flank wound is used as a control. **b**, **c** Comparison of wound area changes from day 0 to day 15 with and without sensing patch ($n = 3$ mice per group). Scale bar, 3 mm. Statistical analysis was performed using two-way repeated measures ANOVA with Sidak's multiple comparisons test (two-sided). Adjusted P values: 1 day, 0.7424; 5 days, 0.9580; 10 days, 0.9992; 15 days, 0.9132. All comparisons ns not significant ($P > 0.05$). H&E tissue section images (**d**) and the statistical data (**e**) of diabetic wounds treated with and without biosensing patch ($n = 4$ mice per group). Basal keratinocyte upward migration thickness, BKUT. Scale bar, 1 mm. Statistical analysis was performed using two-way repeated measures ANOVA with Sidak's multiple comparisons test (two-sided). Adjusted P values: 10 days, 0.5510; 20 days, 0.1916. All comparisons ns not significant ($P > 0.05$). **f** Fluorescence images of CD3 expression in mouse tissue with/without cutted biosensing patch. Scale bar, 50 mm. The experiment was independently repeated three times with similar results. **g** System-level block diagram showing signal transduction, data processing, and wireless transmission. LPF low-pass filter, VF voltage follower, VD voltage divider, TIA transimpedance amplifier, Amp amplifier, LDO low dropout regulator. **h** Photograph of a fully integrated sensing system with mechanical flexibility. Scale bar, 1 cm. **i** Image of a mouse wearing the biosensing system for in situ biochemical and biophysical sensing. **j** Schematic illustration of the wound healing process and the variation of different protein biomarkers in different healing stages. Created in BioRender. Xiao, X. (2025) https://BioRender.com/3m7o2dj. **k** Dynamic changes of TNF-α, IL-6, TGF-β1, VEGF, pH, and temperature during *in-situ* monitoring of infected diabetic wounds ($n = 3$ mice per group). Data are presented as mean ± SD (**c**, **e**, and **k**). Source data from (**c**, **e**, and **k**) are provided as a Source Data file.

potentially due to hypoxia and the generation of lactic acid during the reepithelialization process[67]. Besides, the constant temperatures suggest the absence of infection (Supplementary Fig. 30b), aligning with visual observations.

To further validate the monitoring capability of our sensing patch across different wound types, we conducted additional experiments on infected wounds using a diabetic mouse model with *Staphylococcus aureus* infection (Supplementary Fig. 31). As shown in Fig. 5k, infected wounds diabetic wounds required over 15 days for complete healing, which is significantly longer than the non-infected diabetic wound model. Importantly, the inflammatory cytokines TNF-α and IL-6 maintained persistently higher concentrations throughout the extended healing period compared to non-infected diabetic wounds, demonstrating the characteristic prolonged inflammatory phase that defines chronic wounds. In contrast, anti-inflammatory factors (TGF-β1) and angiogenic factors (VEGF) showed delayed elevation, with gradual increases only after day 8, and concentrations remaining lower than those observed in non-infected wound models (Supplementary Fig. 30b). This pattern confirms the impaired transition from the inflammatory to proliferative and remodeling phases, which is a hallmark of chronic wound pathophysiology. Additionally, the pH value increased by 7.5% on day 4 compared to day 1, which is potentially due to bacterial metabolic activity and altered tissue microenvironment during the infectious process[6,68]. Notably, the temperature in infected diabetic wounds showed a rapid increase on day 4 compared to day 1, with persistently elevated temperatures maintained from days 4 to 12, demonstrating ongoing bacterial burden and systemic inflammatory response[6,68].

Collectively, these findings demonstrate that by utilizing the hydrophilic confinement effect and an auxiliary DNA pre-coating strategy, our multiplexed biosensing platform enables efficient, sensitive, and reliable detection of various biophysical indicators and trace chemical biomarkers in-situ without impeding the wound healing process across different wound types, from non-infected wounds to infected wounds on diabetic mice. This approach provides quantitative and real-time monitoring of various biophysical indicators and low-abundance biomarkers for comprehensive, multidimensional wound evaluation and guides personalized treatment plans for diverse clinical wound conditions.

Discussion

In this work, we report a fully integrated wireless biosensing system comprising a multimodal biosensor array and an electronic circuitry for comprehensive and in-situ monitoring of multiple indicators associated with wound healing. By confining DNA self-circulation amplification in hydrophilic areas and utilizing the inherent stability of tetrahedral DNA structure, this flexible, breathable, and biocompatible biosensing patch enables the sensitive detection of low-abundance and stage-specific proteins, including TNF-α, IL-6, TGF-β1, and VEGF, providing stable monitoring in complex wound environments without disrupting the healing process. Compared to conventional wound monitoring methods, our approach achieves superior sensitivity and stability while enabling real-time, multi-parameter detection. Beyond detection, this platform could guide treatment decisions based on molecular signatures and enable integration with smart dressings for responsive therapeutic delivery.

For successful clinical translation, several technical and practical challenges must be addressed. The current long detection time and disposable sensor design necessitate improvements in reaction kinetics and regeneration capabilities to enhance clinical practicality and cost-effectiveness. Seamless integration with existing healthcare infrastructure will require standardized data formats and intuitive interfaces. Furthermore, continuous biomarker monitoring raises important data privacy considerations, which can be mitigated through robust encryption protocols, HIPAA-compliant data management, and patient-controlled access permissions to ensure secure clinical deployment. In brief, we believe this biosensing strategy marks a significant advance toward practical wound monitoring systems, and further optimization and clinical validation of this technology could facilitate better treatment decisions in clinical settings.

Methods

Materials

Potassium hexacyanoferrate(III) [$K_3Fe(CN)_6$], potassium hexacyanoferrate(II) trihydrate [$K_4Fe(CN)_6{\cdot}3H_2O$], potassium chloride, sodium chloride, bovine serum albumin (BSA), 6-Hydroxy-1-hexanethiol (MCH), ammonium persulphate, polyacrylonitrile (PAN), thermoplastic polyurethane (TPU), octadecyltrichlorosilane (OTS), hexane were purchased from Sigma-Aldrich. Streptozotocin (STZ) was purchased from Bidepharm (Shanghai). Bovine serum albumin-fluorescein isothiocyanate (BSA-FITC) was purchased from Solarbio. Tris(2-carboxyethyl)phosphine hydrochloride (TCEP), Acryl/Bis 30% Solution (29:1), 5 × TBE buffer, 4SGelred, and all the DNA oligonucleotides were purchased from Sangon Biotech. Mouse TNF-α Precoated ELISA kit (Cat. No. 1217202) was purchased from Dakewe Biotech Co., Ltd. NIH/3T3 cells (Cat. No. CRL-1658) and *Staphylococcus aureus* (Cat. No. 23235, strain designation: 494) were purchased from American Type Culture Collection.

Fabrication of nanofiber

To prepare the electrospinning solution, 0.5 g TPU pellets and 0.5 g PAN (Mw = 150,000) were added to N, N-dimethylformamide solvent and stirred at room temperature for 4 days. Electrospinning was carried out using an electrospinning apparatus (Yongkang Leye Technology Development Co., Ltd.) with a volumetric flow rate of 1.25 mL h^{-1}, a tip-to-collect distance of 26 cm, and a voltage of 20 kV. The TPU/PAN fibers were collected on a tin foil for 4 h.

Preparation of Au/nanofiber
A 100-nm-thick gold layer was deposited through a pre-patterned, PET mask by a thermal evaporation system (equipped with evaporation sources, vacuum chamber, thickness monitor, etc., Shenyang Jiuda Vacuum Technology Research Institute, China) under an evaporation rate of 0.3 Å/s.

Preparation of patterned wettable nanofiber
To produce patterned wettability, the Au/nanofiber was soaked in the octadecyltrichlorosilane solution (5 wt.%) for 10 minutes, rinsed twice with alcohol, and dried in air at room temperature to produce a hydrophobic surface. Subsequently, Au/nanofiber covered with a machined PDMS shadow mask was placed inside a plasma cleaner (CPC-B, CIF International Group Co., Ltd) for an oxygen plasma treatment under 200 W for 30 s to prepare a patterned wettable Au/nanofiber.

Preparation of the biochemical sensing array
Equimolar quantities of four strands for the formation of the TDNA (Probe DNA 1-4) were mixed in buffer (20 mM Tris, 50 mM $MgCl_2$, pH 8.0) at 95 °C for 5 min and then cooled to 4 °C, yielding a final concentration of 600 nM. Next, 10 µL of TDNA solution was added to the Au/nanofiber electrode and allowed to incubate overnight at 4 °C. Following rinsed with 10 mM PBS, 1 mM MCH was added to the TDNA/Au/nanofiber electrode to block the nonspecific binding sites. Finally, 10 µL of 1.5 µM H1 was applied to the TDNA/Au/nanofiber electrode and dried in air.

Preparation of Ag/AgCl reference electrode
To prepare the shared reference electrode, a 100-nm thick of silver was sputtered onto the designed reference electrode area. The Ag/AgCl electrode was prepared by performing CV from −1.0 to −0.2 V for 3 cycles at a scan rate of 50 mV s^{-1} using CHI 760E electrochemical workstation (Chenhua, Shanghai, China) in the chlorination solution consisting of 0.01 M HCl and 0.1 M KCl in 0.1 M PBS.

Preparation of pH sensor
To electropolymerize the PANI layer, 0.1 M aniline/0.1 M HCl solution was dropped on the Au/nanofiber, followed by CV from −0.2 to 1 V for 25 cycles at 100 mV s^{-1} using CHI 760E electrochemical workstation.

Water vapor transmission test
WVTR tests were conducted by covering water-containing bottle openings. 1.5 g DI water was put in the bottles, then the patterned Au/nanofiber film was placed to cover the bottles. For comparison, patterned Au/nanofiber film with different raw material ratios, patterned PDMS, and commercial plaster were also used to cover the bottles. At determined time points, the retained mass of the DI water was weighed. The measurements were carried out at 37 °C temperature and 50% humidity.

Human subject recruitment
This study was approved by the Ethics Committee of the First Affiliated Hospital of Nanjing Medical University (Approval No. 2024-SR-1162). All experiment participants were authors of this manuscript, and their participation was conducted with written informed consent. Sex was determined based on self-reporting. One healthy adult female volunteer (39 years old) participated in the thermal dissipation characterization. Explicit consent for the publication of images shown in Fig. 2e was obtained from the participant. Sex and gender were not considered in the study design or analysis as they were not relevant to the technical measurement procedure. The participant has been paid 100 RMB as compensation for the test.

Thermal dissipation characterization
Thermal dissipation characterization was conducted by the infrared thermal imaging camera (Fortic 225, IRS Systems Inc.). Each material was cut into 1.5 × 1.5 cm and attached to the skin of a volunteer on the arm. The area of skin exposed was cleaned and dried prior to attachment. After attaching the materials, the volunteer was allowed to rest for 20 min to allow the skin temperature to equilibrate with the attached material. Thermal images were captured by the infrared thermal imaging camera to monitor the temperature variation across the material-skin interface. For baseline comparison, thermal images of bare skin (without any material attached) were also captured under identical conditions.

Native polyacrylamide gel electrophoresis analysis
To prepare the hydrogel (10%), 4.0 mL of 30% acrylamide/bisacrylamide gel solution (29:1), 2.4 mL of 5 × TBE buffer, 84 µL of 10% persulfuric acid, 4.2 µL of *N,N,N',N'* -tetramethylethylenediamine, and 5.5 mL of DEPC-treated water were mixed thoroughly. The gel was polymerized at room temperature for 90 min. Then, 10 µL of each sample and 2 µL of 6 × DNA loading buffer were added to the native polyacrylamide gel. The native polyacrylamide gel electrophoresis was performed by a Bio-Rad electrophoresis apparatus (PowerPac Basic, BIO-RAD, USA) in 1 × TBE at 80 V for 100 min. After staining in 4S Gelred nucleic acid gel stain solution for 15 min, the gel was imaged using the GeneSys system (Syngene, UK). Uncropped gel images are provided in the Source Data file.

Characterization of the biochemical sensors
SWV, CV, and open circuit potential-EIS were carried out on a CHI760 electrochemical station. All the electrochemical measurements were performed at room temperature, and SWV was performed over a voltage range of −0.5 to −0.05 V at a frequency of 50 Hz. To characterize the sensor performance, a series concentration of TNF-α, IL-6, TGF-β1, and VEGF was spiked in AWF (584.4 mg of NaCl, 336.0 mg of $NaHCO_3$, 29.8 mg of KCl, 27.8 mg of $CaCl_2$, and 3.30 g of BSA in 100 mL of DI water) respectively between the biorecognition interface and working electrode for 90 min of incubation. The LOD was calculated on the basis of the mean of the blank, the standard deviation of the blank, the sensitivity, and a defined confidence factor of 3.2 (for a confidence of 95%).

To characterize surface modification after each step electrochemically, CV and open circuit potential–EIS readings were obtained in 0.1 M KCl, containing 5.0 mM of $K_4Fe(CN)_6/K_3Fe(CN)_6$ (1:1) under the following conditions: potential range, −0.1 V to 0.6 V; scan rate, 20 mV s^{-1}; frequency range, 0.1–100 kHz; amplitude, 5 mV.

SWV was used to assess the sensing performances of multiplexed biochemical sensors under the following conditions: potential range, −0.5 V to −0.05 V; scan rate, 20 mV s^{-1}; frequency range, 0.1–100 kHz; amplitude, 5 mV.

The long-term stability of the biosensors was evaluated by storing them at 4 °C with a relative humidity (RH) of 10%, and their performance was monitored weekly over four weeks.

Biochemical data analysis and concentration calculation
Protein concentrations were calculated from SWV peak currents using linear calibration curves established with standard protein solutions in AWF. The calibration equations for each protein biomarker were as follows:

$$\mathrm{TNF}-\alpha: i = 1.5112 + 0.0009c\,(R^2 = 0.9858)$$

$$\mathrm{IL}-6: i = 1.2987 + 0.0383c\,(R^2 = 0.9924)$$

$$\mathrm{TGF}-\beta1: i = 1.469 + 0.0481c\ (R^2 = 0.9902)$$

$$\mathrm{VEGF}: i = 1.2771 + 0.2427c\ (R^2 = 0.9899)$$

where c (TNF-α and TGF-β1: pg mL^{-1}, IL-6 and VEGF: ng mL^{-1}) represents the protein concentration and i (μA) represents the SWV peak current. These calibration curves were also used in the smartphone application to convert real-time electrochemical signals to protein concentrations during *in-situ* wound monitoring.

Characterization of the biophysical sensors

The pH sensor was characterized by measuring the OCP response in buffer solutions with pH values ranging from 4 to 10. Calibration curves were obtained by recording the OCP at each pH value after stabilization. The temperature sensor characterization was performed by monitoring the resistance change of the serpentine metal resistor as a function of temperature from 35 to 45 °C using a temperature-controlled chamber.

Cytocompatibility evaluation

CCK-8 assay (Cat No. KGA9305-500, Jiangsu Keygen Biotech. Co., Ltd.) was used to assess the cytocompatibility of different materials to NIH/3T3 cells. NIH/3T3 cells (5000 cells per well) were cultured in a 96-well plate at 37 °C in a 5% CO_2 atmosphere for 12 h. Then, nanofiber, Au/nanofiber, TDNA/Au/nanofiber, and H1/TDNA/Au/nanofiber were added to NIH/3T3 cells (duplicated samples, $n = 6$), respectively, and incubated for 24 h. After removing the culture supernatants, 100 μL of fresh DMEM and 10 μL of CCK-8 were added to a new 96-well plate. 3 h later, the absorbance (Abs) at 450 nm of each well was recorded. DMEM was set as the control group.

Cell viability ratio (%) was calculated using the following formula

$$\text{Cell viability}(\%) = Abs_{sample}/Abs_{control} \times 100\%$$

Hemocompatibility assessment

The hemocompatibilities of different materials were evaluated by the hemolysis ratio. The extracts (20 mg mL^{-1}) of nanofiber, Au/nanofiber, TDNA/Au/nanofiber, and H1/TDNA/Au/nanofiber were prepared by soaking in PBS at 37 °C for 24 h. Red blood cells (RBCs) were separated from the fresh citrate-anticoagulated rat whole blood (3.8% sodium citrate/blood, 1/9 v/v) by centrifugation at 1000 × g for 10 min. The RBCs were rinsed and centrifuged using PBS three times and a suspension of RBC (5 vol%) in PBS was obtained. The mixtures of RBC suspension and the different extract dilutions (1:1 v/v) were, respectively, incubated at 37 °C for three hours. Next, the mixtures were centrifuged at 1000 × g for 10 min, and the supernatants were ready for testing (duplicated samples, $n = 4$). Abs at 540 nm of each supernatant was recorded. Ultrapure H_2O and PBS were set as the positive control (PC) and negative control (NC), respectively. The hemolysis ratio (%) was given by the following formula

$$\text{Hemolysis ratio}(\%) = \left(Abs_{sample} - Abs_{NC}\right)/\left(Abs_{PC} - Abs_{NC}\right) \times 100\%$$

Murine non-infection wound model

Male outbred mice (C57BL/6), which were 6 weeks old and weighing 20–25 g were used in this study. All mice were housed under standard laboratory conditions with a 12/12-h light/dark cycle, ambient temperature of 18–24 °C, and humidity of 40–60%. Diabetic mice were injected subcutaneously with streptozotocin (50 mg kg^{-1}) before wounding and daily for 3 days after wounding and on days of sensor placement to induce Type 1 diabetes (the blood glucose levels consistently exceeded 16.7 mmol L^{-1}). To evaluate the biocompatibility of the sensing device for real-time wound assessment, animals were subjected to anesthesia and analgesic treatment before creating bilateral symmetrical full-thickness skin defects measuring 6 mm in diameter on the dorsal surface at day −1. These wounds were positioned equidistantly from the spinal midline. The right-sided wound was treated with a fragmented 4 mm × 4 mm sensing patch placed in direct contact with the wound bed, while the contralateral wound functioned as an untreated control.

Murine infection wound model

The in vivo evaluation was performed utilizing a diabetic wound model established in 9-week-old male db/db mice (BKS.Cg-Dock7m +/+ Leprdb/J), a well-established Type 2 diabetic mouse strain. Mice were maintained under standard housing conditions with a 12/12-h light/dark cycle, ambient temperature of 18–24 °C, and humidity of 40–60%. The wound creation protocol followed identical procedures to the uninfected model except for the bacterial suspension (50 μL containing 10^6 CFU/mL *Staphylococcus aureus*) that was inoculated onto the wound surface on day 0.

Wound monitoring in mouse models

To visually characterize the effect of the sensing patch on wound healing, photographs of the wounds in both the experimental and control groups were taken, and the wound healing area was measured.

For the H&E staining, at days 1 and 20, mice were euthanized via CO_2 inhalation, and the dorsal skin was carefully excised as a single large section and laid flat on a smooth card. Wounds were dissected out, fixed in 4% paraformaldehyde for a minimum of 24 h, and stored at 4 °C. Following fixation, samples were placed in 70% (v/v) ethanol for 24 h before being processed in a HistoCore PEARL tissue processor (Leica). Tissue samples were sequentially passed through an ethanol gradient (70%, 80%, 95%, and 100% × 3 cycles, each for 45 min at 45 °C), followed by xylene treatment (3 cycles of 45 min each at 45 °C), and finally embedded in paraffin (3 cycles of 45 min each at 62 °C) using the HistoCore Arcadia C and H paraffin embedder (Leica). Thin tissue sections (4 μm) were then prepared using a Leica CM1950 microtome and mounted onto Polysine slides. Slides were dried at 40 °C for at least one hour prior to staining. H&E staining was carried out using a Leica Autostainer XL, and slides were mounted with Organo mounting medium. For the in-situ monitoring, the wearable biosensing system was placed on the wound and wirelessly communicated the multiplexed sensing data to the user interface, enabling comprehensive recordings of TNF-α, IL-6, TGF-β1, VEGF, pH, and temperature measurements.

In-situ wound monitoring was conducted on diabetic mouse models. The flexible biosensing device was positioned directly onto the wound bed, ensuring complete contact between the sensing electrodes and wound exudate. The patch was secured using a transparent medical adhesive film that maintained sensor stability while permitting visual wound inspection. Real-time measurements of protein biomarkers (TNF-α, IL-6, TGF-β1, VEGF) and biophysical parameters (pH, temperature) were wirelessly transmitted to the custom mobile interface. Signal processing and data visualization were performed using custom algorithms detailed in Supplementary Code. A new disposable sensor patch was used for each measurement session (day 1, 2, 3, and 4 for non-infected wounds; day 1, 4, 8, and 12 for infected wounds) throughout the monitoring period.

Statistics and reproducibility

At least three independent experiments of each type have been done and have produced consistent results. All data were presented as the means with standard errors (SD). The statistical significance was evaluated using a two-way repeated measures ANOVA with Sidak's multiple comparisons test (two-sided) in GraphPad Prism 8 software. $P > 0.05$

was considered statistically not significant. No statistical method was used to predetermine sample size. No data were excluded from the analyses. The experiments were not randomized. The investigators were not blinded to allocation during experiments and outcome assessment.

Ethical statement

All animal procedures were conducted in accordance with protocol IACUC-JSAB25012M, approved by the Animal Ethics Committee of Aniphe Biolaboratory Inc. (Nanjing, China). The thermal dissipation characterization involving a human research participant was conducted under protocol 2024-SR-1162, approved by the Ethics Committee of the First Affiliated Hospital of Nanjing Medical University. Written informed consent was obtained.

Reporting summary

Further information on research design is available in the Nature Portfolio Reporting Summary linked to this article.

Data availability

The authors declare that data supporting the findings of this study are available within the article and its Supplementary Information files. Source data are provided with this paper.

Code availability

The data processing algorithms, signal conversion formulas, and user interface implementation details are provided as Supplementary Code. Concentration calculations are performed using standard calibration curves as described in the manuscript.

References

1. Vartanian, A. Diabetic wound dressings. *Nat. Rev. Mater.* **9**, 92–92 (2024).
2. Maschalidi, S. et al. Targeting SLC7A11 improves efferocytosis by dendritic cells and wound healing in diabetes. *Nature* **606**, 776–784 (2022).
3. Falanga, V. et al. Chronic wounds. *Nat. Rev. Dis. Prim.* **8**, 50 (2022).
4. Church, D., Elsayed, S., Reid, O., Winston, B. & Lindsay, R. Burn wound infections. *Clin. Microbiol Rev.* **19**, 403–434 (2006).
5. Wang, C., Shirzaei Sani, E. & Gao, W. Wearable bioelectronics for chronic wound management. *Adv. Funct. Mater.* **32**, 2111022 (2022).
6. Jiang, Y. et al. Wireless, closed-loop, smart bandage with integrated sensors and stimulators for advanced wound care and accelerated healing. *Nat. Biotechnol.* **41**, 652–662 (2023).
7. Zheng, X. T. et al. Battery-free and AI-enabled multiplexed sensor patches for wound monitoring. *Sci. Adv.* **9**, eadg6670 (2023).
8. Wang, C. et al. Wound management materials and technologies from bench to bedside and beyond. *Nat. Rev. Mater.* **9**, 550–566 (2024).
9. Shin, Y. et al. Low-impedance tissue-device interface using homogeneously conductive hydrogels chemically bonded to stretchable bioelectronics. *Sci. Adv.* **10**, eadi7724 (2024).
10. Ge, Z. et al. Wireless and closed-loop smart dressing for exudate management and on-demand treatment of chronic wounds. *Adv. Mater.* **35**, 2304005 (2023).
11. Shirzaei Sani, E. et al. A stretchable wireless wearable bioelectronic system for multiplexed monitoring and combination treatment of infected chronic wounds. *Sci. Adv.* **9**, eadf7388 (2023).
12. Xu, Z. et al. Cellulose-based pH-responsive janus dressing with unidirectional moisture drainage for exudate management and diabetic wounds healing. *Adv. Funct. Mater.* **34**, 2307449 (2024).
13. Werner, S. & Grose, R. Regulation of wound healing by growth factors and cytokines. *Physiol. Rev.* **83**, 835–870 (2003).
14. Peña, O. A. & Martin, P. Cellular and molecular mechanisms of skin wound healing. *Nat. Rev. Mol. Cell Biol.* **25**, 599–616 (2024).
15. Tu, J. et al. A wireless patch for the monitoring of C-reactive protein in sweat. *Nat. Biomed. Eng.* **7**, 1293–1306 (2023).
16. Clifford, A. et al. Strategies for biomolecular analysis and continuous physiological monitoring. *J. Am. Chem. Soc.* **143**, 5281–5294 (2021).
17. Flynn, C. D. et al. Biomolecular sensors for advanced physiological monitoring. *Nat. Rev. Bioeng.* **1**, 560–575 (2023).
18. Zhang, J. et al. Weakly ionized gold nanoparticles amplify immunoassays for ultrasensitive point-of-care sensors. *Sci. Adv.* **10**, eadn5698 (2024).
19. Arwani, R. T. et al. Stretchable ionic–electronic bilayer hydrogel electronics enable in situ detection of solid-state epidermal biomarkers. *Nat. Mater.* **23**, 1115–1122 (2024).
20. Li, J. et al. A tissue-like neurotransmitter sensor for the brain and gut. *Nature* **606**, 94–101 (2022).
21. Peng, X. et al. A breathable, biodegradable, antibacterial, and self-powered electronic skin based on all-nanofiber triboelectric nanogenerators. *Sci. Adv.* **6**, eaba9624 (2020).
22. Vining, K. H. & Mooney, D. J. Mechanical forces direct stem cell behaviour in development and regeneration. *Nat. Rev. Mol. Cell Biol.* **18**, 728–742 (2017).
23. Dong, Y., Fu, S., Yu, J., Li, X. & Ding, B. Emerging smart micro/nanofiber-based materials for next-generation wound dressings. *Adv. Funct. Mater.* **34**, 2311199 (2024).
24. Wang, L. et al. Robust dual equivariant gradient antibacterial wound dressing-loaded artificial skin with nano-chitin particles via an electrospinning-reactive strategy. *Adv. Fiber Mater.* **7**, 204–218 (2025).
25. Singh, S. et al. Recent advancements in polyurethane-based tissue engineering. *ACS Appl. Bio Mater.* **6**, 327–348 (2023).
26. Pakyari, M., Farrokhi, A., Maharlooei, M. K. & Ghahary, A. Critical role of transforming growth factor beta in different phases of wound healing. *Adv. Wound Care* **2**, 215–224 (2013).
27. Goswami, A. G. et al. An appraisal of vascular endothelial growth factor (VEGF): the dynamic molecule of wound healing and its current clinical applications. *Growth Factors* **40**, 73–88 (2022).
28. Cobb, B. D. & Ciarkson, J. M. A simple procedure for optimising the polymerase chain reaction (PCR) using modified Taguchi methods. *Nucleic Acids Res.* **22**, 3801–3805 (1994).
29. Zhu, Y., Wu, J. & Zhou, Q. Functional DNA sensors integrated with nucleic acid signal amplification strategies for non-nucleic acid targets detection. *Biosens. Bioelectron.* **230**, 115282 (2023).
30. Tomita, N., Mori, Y., Kanda, H. & Notomi, T. Loop-mediated isothermal amplification (LAMP) of gene sequences and simple visual detection of products. *Nat. Protoc.* **3**, 877–882 (2008).
31. Ye, C., Lukas, H., Wang, M., Lee, Y. & Gao, W. Nucleic acid-based wearable and implantable electrochemical sensors. *Chem. Soc. Rev.* **53**, 7960–7982 (2024).
32. Nguyen, P. Q. et al. Wearable materials with embedded synthetic biology sensors for biomolecule detection. *Nat. Biotechnol.* **39**, 1366–1374 (2021).
33. Ates, H. C. et al. End-to-end design of wearable sensors. *Nat. Rev. Mater.* **7**, 887–907 (2022).
34. Gao, H. et al. Leaf-inspired patterned organohydrogel surface for ultrawide time-range open biosensing. *Adv. Sci.* **10**, 2207702 (2023).
35. Tehrani-Bagha, A. R. Waterproof breathable layers – a review. *Adv. Colloid Interface Sci.* **268**, 114–135 (2019).
36. Mustapha, R., Zoughaib, A., Ghaddar, N. & Ghali, K. Modified upright cup method for testing water vapor permeability in porous membranes. *Energy* **195**, 117057 (2020).
37. Huang, Q. & Zheng, Z. Pathway to developing permeable electronics. *ACS Nano* **16**, 15537–15544 (2022).

38. Bialy, R. M., Mainguy, A., Li, Y. & Brennan, J. D. Functional nucleic acid biosensors utilizing rolling circle amplification. *Chem. Soc. Rev.* **51**, 9009–9067 (2022).
39. Zhang, Z., Sen, P., Adhikari, B. R., Li, Y. & Soleymani, L. Development of nucleic-acid-based electrochemical biosensors for clinical applications. *Angew. Chem. Int Ed.* **61**, e202212496 (2022).
40. Gines, G. et al. Functional analysis of single enzymes combining programmable molecular circuits with droplet-based microfluidics. *Nat. Nanotechnol.* **19**, 800–809 (2024).
41. Wang, X., Dai, C., Wu, Y., Liu, Y. & Wei, D. Molecular-electrome chanical system for unamplified detection of trace analytes in biofluids. *Nat. Protoc.* **18**, 2313–2348 (2023).
42. Lin, M. et al. Programmable engineering of a biosensing interface with tetrahedral DNA nanostructures for ultrasensitive DNA detection. *Angew. Chem. Int Ed.* **54**, 2151–2155 (2015).
43. Song, P. et al. Programming bulk enzyme heterojunctions for biosensor development with tetrahedral DNA framework. *Nat. Commun.* **11**, 838 (2020).
44. Gao, Y. et al. A flexible multiplexed immunosensor for point-of-care in situ wound monitoring. *Sci. Adv.* **7**, eabg9614 (2021).
45. Xiao, Y., Lai, R. Y. & Plaxco, K. W. Preparation of electrode-immobilized, redox-modified oligonucleotides for electrochemical DNA and aptamer-based sensing. *Nat. Protoc.* **2**, 2875–2880 (2007).
46. Li, Y. et al. In vivo imaging of mitochondrial DNA mutations using an integrated nano Cas12a sensor. *Nat. Commun.* **14**, 7722 (2023).
47. Bendixen, K. K. et al. A qPCR technology for direct quantification of methylation in untreated DNA. *Nat. Commun.* **14**, 5153 (2023).
48. Tang, Y. et al. A CRISPR-based ultrasensitive assay detects attomolar concentrations of SARS-CoV-2 antibodies in clinical samples. *Nat. Commun.* **13**, 4667 (2022).
49. Qian, R. et al. Rectifying artificial nanochannels with multiple interconvertible permeability states. *Nat. Commun.* **15**, 2051 (2024).
50. Lovrić, M. Square-wave voltammetry. In *Electroanalytical Methods: Guide to Experiments and Applications* (Springer Berlin Heidelberg, 2010).
51. Ramaley, L. & Krause, M. S. Theory of square wave voltammetry. *Anal. Chem.* **41**, 1362–1365 (1969).
52. Pei, H. et al. A DNA nanostructure-based biomolecular probe carrier platform for electrochemical biosensing. *Adv. Mater.* **22**, 4754–4758 (2010).
53. Wang, L. et al. Rapid and ultrasensitive electromechanical detection of ions, biomolecules and SARS-CoV-2 RNA in unamplified samples. *Nat. Biomed. Eng.* **6**, 276–285 (2022).
54. Shan, L. et al. Tetrahedral DNA nanostructure-engineered paper-based sensor with an enhanced antifouling ability for photoelectrochemical sensing. *Anal. Chem.* **95**, 4760–4767 (2023).
55. Jiang, C. et al. Antifouling strategies for selective in vitro and in vivo sensing. *Chem. Rev.* **120**, 3852–3889 (2020).
56. Zhang, T. et al. Design, fabrication and applications of tetrahedral DNA nanostructure-based multifunctional complexes in drug delivery and biomedical treatment. *Nat. Protoc.* **15**, 2728–2757 (2020).
57. Martins, A. S. G. et al. Enhancing neuronal cell uptake of therapeutic nucleic acids with tetrahedral DNA nanostructures. *Small* **20**, 2309140 (2024).
58. Ye, C. et al. A wearable aptamer nanobiosensor for non-invasive female hormone monitoring. *Nat. Nanotechnol.* **19**, 330–337 (2024).
59. Zhao, X., He, G., Deng, W., Tan, Y. & Xie, Q. Tailoring enzymatic loading capacity on 3D macroporous gold by catalytic hairpin assembly and hybridization chain reaction: Application for ultrasensitive self-powered microRNA detection. *Biosens. Bioelectron.* **219**, 114813 (2023).
60. Grellner, W., Georg, T. & Wilske, J. Quantitative analysis of proinflammatory cytokines (IL-1β, IL-6, TNF-α) in human skin wounds. *Forensic. Sci. Int.* **113**, 251–264 (2000).
61. Fierheller, M. & Sibbald, R. G. A clinical investigation into the relationship between increased periwound skin temperature and local wound infection in patients with chronic leg ulcers. *Adv. Skin Wound Care* **23**, 369–379 (2010).
62. Darvishi, S. et al. Advances in the sensing and treatment of wound biofilms. *Angew. Chem. Int Ed.* **61**, e202112218 (2022).
63. Xiao, J., Zhou, Z., Zhong, G., Xu, T. & Zhang, X. Self-sterilizing microneedle sensing patches for machine learning-enabled wound pH visual monitoring. *Adv. Funct. Mater.* **34**, 2315067 (2024).
64. Schreml, S. et al. The impact of the pH value on skin integrity and cutaneous wound healing. *J. Eur. Acad. Dermatol. Venereol.* **24**, 373–378 (2010).
65. Behm, B., Babilas, P., Landthaler, M. & Schreml, S. Cytokines, chemokines and growth factors in wound healing. *J. Eur. Acad. Dermatol. Venereol.* **26**, 812–820 (2012).
66. Brown, R. L., Ormsby, I., Doetschman, T. C. & Greenhalgh, D. G. Wound healing in the transforming growth factor-β1—deficient mouse. *Wound Repair Regen.* **3**, 25–36 (1995).
67. Wallace, L. A., Gwynne, L. & Jenkins, T. Challenges and opportunities of pH in chronic wounds. *Ther. Deliv.* **10**, 719–735 (2019).
68. Wang, C. et al. A microfluidic wearable device for wound exudate management and analysis in human chronic wounds. *Sci. Transl. Med.* **17**, eadt0882 (2025).

Acknowledgements

This study was supported by the National Natural Science Foundation of China (62201286, T.W., 62301283, X.Z., and 22405131, T.L.), Natural Science Foundation for Excellent Young Scholars (62322108, T.W.), Program of Jiangsu Specially-Appointed Professor, Science Foundation of Nanjing University of Post and Telecommunications (NY221004, T.W.), U35 Strong Foundation Project in Nanjing (2024U35-03, T.W.), Natural Science Research Start-up Foundation of Recruiting Talents of Nanjing University of Posts and Telecommunications (NY222099, X.Z.), Jiangsu Funding Program for Excellent Postdoctoral Talent (2023ZB587, X.Z.).

Author contributions

X. Zhao and T. Wang conceive the project, design the studies and analyze the results. X. Zhao, J. Huang, B. Yang, Z. Hu, H. Zou, S. Liu, and Q. He conduct the experiments. J. Zhang, X. Ma, and C. Jiang contribute to the murine infection wound model. X. Zhao write the manuscript. T. Wang, T. Li, L. Weng, and L. Wang revise the manuscript. T. Wang, and L. Wang supervise and revise the project.

Competing interests

The authors declare no competing interests.

Additional information

Supplementary information The online version contains supplementary material available at https://doi.org/10.1038/s41467-025-63927-9.

Correspondence and requests for materials should be addressed to Ting Wang or Lianhui Wang.

Peer review information *Nature Communications* thanks the anonymous reviewers for their contribution to the peer review of this work. A peer review file is available.